Free-Stream Effects on Jet-Installation Noise of a Dual-Stream Engine

Falcão Loureiro Rêgo, Leandro; Avallone, Francesco; Ragni, Daniele; Casalino, Damiano; van der Velden, Wouter

DOI
10.2514/6.2019-2491

Publication date
2019

Document Version
Final published version

Published in
25th AIAA/CEAS Aeroacoustics Conference

Aeroacoustics Conferences
20-23 May 2019, Delft, The Netherlands
25th AIAA/CEAS Aeroacoustics Conference

10.2514/6.2019-2491

Free-Stream Effects on Jet-Installation Noise of a Dual-Stream Engine

Leandro Rego*, Francesco Avallone†, Daniele Ragni‡ and Damiano Casalino§
Delft University of Technology, Delft, 2629HS, The Netherlands

Wouter van der Velden¶
Dassault Systemes Deutschland GmbH, Curiestraße 4, 70563, Stuttgart, Germany

An investigation of the effects of free-stream on jet-installation noise is performed using a numerical solver based on the lattice-Boltzmann method. In order to simulate a realistic configuration, a high-lift wing comprised by a main element and a deployed flap (MD30P30N) is placed in the vicinity of a dual-stream engine (GE90-94B). The engine operating parameters are used as inputs to generate realistic exhaust flows. Far-field noise spectra from the isolated and installed jets, obtained through the Ffowcs-Williams and Hawkings analogy, are compared for different polar angles. In the absence of free-stream, the results show a low-frequency noise amplification, occurring mainly upstream of the jet axis. This noise increase is due to a dipole source at the flap trailing-edge, where hydrodynamic waves from the jet scatter as sound to the far-field. With free-stream, the wing produces a downward flow, which deflects the jet plume. There is a consequent change on the shear layer turbulence characteristics, which is responsible for altering the far-field spectral shape and directivity pattern of the overall configuration. Through a wavelet decomposition of the near-pressure field, coherent and chaotic fluctuations are splitted. Near-field spectra show the change in amplitude of fluctuations of coherent structures due to free-stream, which are in agreement with the far-field results.

Nomenclature

c	=	speed of sound [m/s]
D	=	exit plane external diameter [m]
f	=	frequency [Hz]
M	=	Mach number
M_a	=	acoustic Mach number
$\dot{m}$	=	mass-flow [kg/s]
p	=	static pressure [Pa]
St	=	Strouhal number
T	=	temperature [K]
u	=	time-averaged axial velocity ($x-$direction) [m/s]
u'	=	root-mean-square axial velocity fluctuations ($x-$direction) [m/s]
U	=	velocity magnitude [m/s]
θ	=	polar angle of the observer [°]
Subscripts		
B	=	bypass jet flow
C	=	core jet flow
f	=	free-stream

*PhD Candidate, Aerodynamics, Wind Energy, Flight Performance and Propulsion Department, l.rego@tudelft.nl, AIAA Student Member
†Assistant Professor, Aerodynamics, Wind Energy, Flight Performance and Propulsion Department, f.avallone@tudelft.nl, AIAA member
‡Assistant Professor, Aerodynamics, Wind Energy, Flight Performance and Propulsion Department, d.ragni@tudelft.nl, AIAA member
§Professor, Aerodynamics, Wind Energy, Flight Performance and Propulsion Department, d.casalino@tudelft.nl, AIAA member
¶Solution Consultant, SIMULIA A&D, CoE, Experience Management, wouter.vandervelden@3ds.com, AIAA member

I. Introduction

High bypass turbofan engines provide significant benefits in terms of fuel burn and jet noise reduction due to their lower exhaust velocity [1]. However, these engines have large diameters so that a higher mass flow can generate the necessary amount of thrust. Therefore, due to their size, they have to be mounted closer to the wing to maintain a minimum ground clearance. The increased proximity results in interactions between the jet flow and a nearby airframe surface, generating an additional noise source known as Jet-Installation Noise (JIN) [2]. The JIN is especially significant during take-off and approach flight conditions, when the deployed high-lift systems are positioned close to the jet [3]. Therefore, the phenomena behind engine installation effects must be accurately modeled so that appropriate noise reduction solutions can be developed.

The interaction between a jet and a nearby semi-infinite solid surface was first investigated by Ffowcs-Williams and Hall [4]. For a surface outside of the plume, they showed that hydrodynamic pressure fluctuations from the jet are scattered as sound to the far-field at the surface trailing-edge. It was found that the sound intensity produced by this source scales with the fifth power of the jet velocity, thus becoming relevant at subsonic Mach numbers. It was also shown that the noise increase occurs at low and mid frequencies, followed by either reflection or shielding of acoustic waves at higher frequencies [5]. The sound directivity patterns were found to be consistent with a dipole source: in the azimuthal direction, there were two lobes with peaks in the directions normal to the surface, whereas in the surface plane there was no noise increase. In the polar direction, a cardioid pattern was obtained, with the maximum noise amplification in the upstream direction of the jet. At low polar angles, towards the jet axis in the downstream direction, noise levels similar to the ones of the isolated configuration were obtained [5].

In analytical formulations, JIN is usually modeled with the characteristics of a single-stream jet flow and a nearby flat plate, representing the airframe surface. These models can capture very well the effects of trailing-edge scattering of jet hydrodynamic waves, since they use an exact tailored Green's function to solve the problem of scattering by a half plane [6–8]. While these models provide fast-running predictions, there is often a trade-off in terms of geometric simplification. For the investigation of more complex geometries, comprised for example by dual-stream jets and high-lift wings, wind tunnel tests are usually performed [9–11]. There are, however, some shortcomings with those JIN experiments, such as the model scale, the temperature of the core jet, or the presence of external flow. Therefore, JIN investigations that take into account all these characteristics are lacking in the literature.

The main focus of this work is then to assess the effect of free-stream on the noise produced by an installed dual-stream engine at realistic operating conditions. Wind tunnel tests carried out by Proença [12] show that the addition of free-stream around a jet results in an increase of the potential core length and a reduction of the turbulence levels in the jet shear layer. Consequently, there is a reduction of installed noise levels and the spectral peak shifts to higher frequencies. However, these studies were carried out with flat plates and symmetrical airfoils. It is likely that a cambered airfoil in the vicinity of a jet produces a downward velocity component, affecting the jet development and the overall noise characteristics.

To assess this effect, realistic geometries are necessary. In this work, the installed jet setup is comprised by a dual-stream nacelle (from the GE90-94B engine) and a high-lift wing; the MD30P30N. These geometries are chosen since they are publicly available for research purposes [13, 14]. This setup allows for an investigation on full-scale models, with inputs taken from actual engine operating parameters, so that a take-off condition can be modeled. Co-axial jet flows comprised by a hot core and a cold bypass are also obtained from this model, adding to the realism and complexity of the analysis.

The most appropriate way to conduct such investigations is through a numerical approach, since there would be high costs for a full-scale testing of this configuration. The calculations are performed with a software that employs the lattice-Boltzmann method, coupled with a Very Large Eddy Simulation model (LBM-VLES). This method has been chosen since high-fidelity simulations can be carried out with a relatively low computational cost. Highly accurate results can obtained through this methodology, when compared to experimental data, as shown earlier by van der Velden et al. [15], Rego et al. [16] and Nickerson et al. [17] for isolated, installed and chevron single-stream jets, respectively.

This paper is organized as follows. The computational methodology is addressed in Section II. The characteristics of the model setup are reported in section III, with a description of the geometry and flow conditions. The installation effects are addressed in Section IV in the absence of free-stream. In Section V, the effect of free-stream is discussed with a correlation between near- and far-fields performed through a wavelet decomposition. Finally, the concluding remarks are presented in Section VI.

II. Methodology

The lattice-Boltzmann method (LBM) solves the discrete form of the Boltzmann equation by using particle distribution functions to simulate the macro flow properties. The fluid properties such as density, momentum and internal energy are obtained through a local integration of the particle distribution [18]. The solution of the Boltzmann equation is performed on a Cartesian mesh (lattice), with an explicit time integration and collision model. The distribution functions are projected on a basis of Hermite polynomials and the moments are computed over a discrete set of particle velocities, using Gaussian quadrature formulas for different lattices [19]. For this work, a 19-state lattice, known as D3Q19, is adopted. A Very Large Eddy Simulation (VLES) model accounts for the unresolved scales of turbulence through an eddy-viscosity turbulence model. A modified two-equations $k-\epsilon$ Renormalization Group (RNG) turbulence model is employed to compute a turbulent relaxation time that is added to the viscous relaxation time [20].

The far-field noise is computed through the Ffowcs-Williams and Hawkings analogy [21], adopting the formulation 1A from Farassat extended to a convective wave equation [22, 23]. The formulation is implemented in the time domain using a source-time dominant algorithm [24]. A permeable surface is defined encompassing the jet and the wing, where pressure and velocity fluctuations are recorded and used for far-field noise estimation. A more detailed description of the FWH surface is reported in section III. In addition, the FWH analogy is applied using pressure fluctuations on the wing surfaces, in order to isolate the noise contribution from the acoustic dipoles.

The methodology described above is implemented in the commercial software Simulia PowerFLOW 6-2019. This software has been also used and validated for aero-engine aeroacoustic applications to predict fan broadband noise in subsonic [25, 26] and transonic conditions [27]. A validation study for an isolated jet (SMC000) has been accomplished by van der Velden et al. [15], showing a very good agreement with experimental results, as well as Nickerson et al. [17] for an isolated jet with chevron nozzles. For an installed configuration, computations were performed by Rego et al. [16] with a flat plate in the vicinity of a single-stream jet. The results agreed with experimental data, and they were used for correlations between the near-field phenomena and the resultant noise in the far-field due to installation effects.

III. Computational Setup

A. Geometry and Discretization

As stated in section I, the aim of this work is to carry out an investigation of the effects of free-stream on the noise generated by an installed jet. A dual-stream engine configuration is chosen for a more realistic analysis, so that both core and bypass exhaust flows are simulated. The GE90-94B is selected since its geometry is publicly available for research purposes, and it has been used in operating aircraft. Engine parameters, such as intake mass-flow, bypass ratio and flow temperatures at take-off condition [13] are available to be used as input for the simulations. This model also allows for full-scale jet-installation noise analyses. Since only the exhaust flows are of importance to this work, the internal engine components such as the compressor, fan and turbines are removed, while only the inner and outer walls are kept. The engine cross-section is shown in Fig. 1, along with its dimensions.

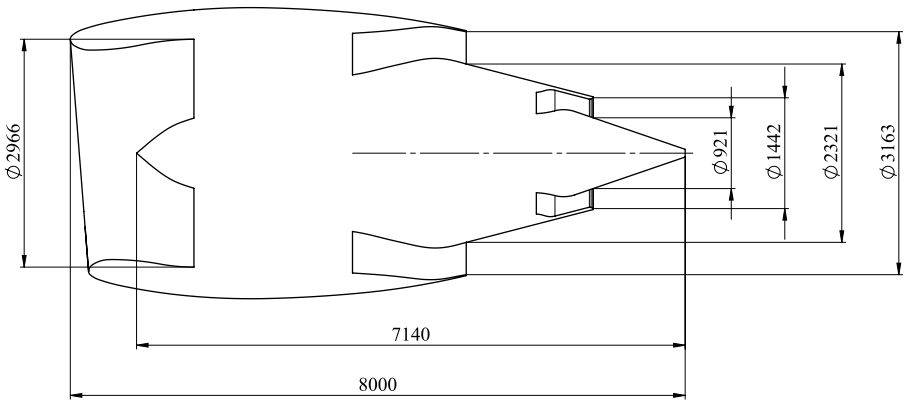

Fig. 1 GE90-94B engine cross-section and dimensions (in mm)

To model the installation effects, a 2.5D wing configuration with a deployed flap is placed in the vicinity of the engine. The high-lift wing selected is the MD30P30N, which has been extensively used for airframe noise investigations

[14]. The geometry of the wing is also publicly available, and it is comprised of a main element, a slat and a flap, both deflected of 30°, relative to the chord-line. For the simulations, the slat is removed since it does not contribute to the jet-installation effects, and the simulations are carried out at zero angle of attack. Moreover, without the slat, the computational cost can be reduced. The wing is scaled based on the engine dimensions, with a chord length of $3D_B$. Its position is defined based on the distance between the flap trailing-edge and the jet axis, as shown in Fig. 2. The span of the wing is defined as $25D_B$ to avoid side-edge scattering.

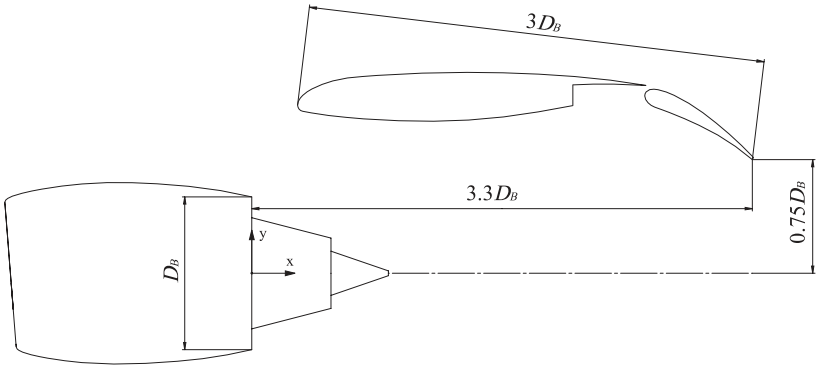

Fig. 2 Wing dimensions and flap trailing-edge position, relative to the engine

The computational domain is divided into regions with different mesh refinements (Variable Resolution - VR), with a change in element size by a factor of 2, for adjacent regions. A global mesh resolution is then defined, based on the number of elements in a characteristic length (bypass exit diameter). In this work, a resolution of 32 is used. The resultant element size is used throughout the jet plume. Further levels of refinement are added downstream of the engine lips to properly capture the formation of the shear layers and the hydrodynamic fluctuations. There is a progressive coarsening of the grid towards the far-field boundaries, which contributes to the damping of acoustic waves, reducing the effects from reflection. An acoustic sponge, which consists in a region of increased viscosity, is also added around the entire geometry to prevent wave reflection at the walls of the computational domain [28].

B. Boundary Conditions

The computational setup is comprised by the dual-stream engine and the flapped wing, which are placed in a volumetric domain. In total, four cases are simulated: isolated and installed engine configurations, both with and without free-stream. To generate the core and bypass jets, inlet boundary conditions are set on disks upstream of their respective exit planes. An outlet boundary condition is also set on a disk representing the fan plane, with a prescribed intake mass-flow. The boundary planes are shown in Fig. 3a, where the fan outlet is shown in green, and the bypass and core inlets are shown in blue and red, respectively. The inlets are set at positions upstream of the respective exit planes, as shown in Fig. 3b, to avoid affecting the jet development. This strategy has been already adopted by Blumenthal et al. [29], for CFD analyses with the GE90 engine.

(a) **(b)**

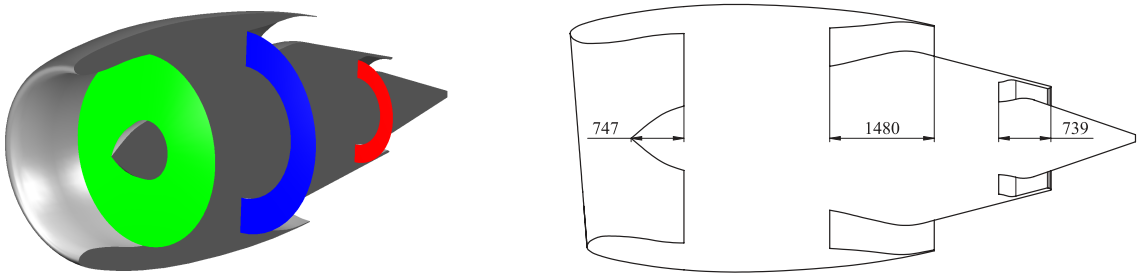

Fig. 3 Boundary planes inside the engine to generate the intake flow (green), bypass (blue) and core (red) jets. (Dimensions in mm)

The properties of the boundary planes in the engine are set based on mass-flow and temperature, and they are the same for all cases. A mass-flow rate of 1350 kg/s is divided into bypass and core flows, with a bypass ratio of 8.4, consistent with a take-off condition [13]. The fan and bypass flows are kept at ambient temperature $T_a = 293$ K, whereas the core jet has a temperature $T_C = 800$ K, or $T_C = 2.7T_a$. An ambient pressure $p_a = 101235$ Pa is also adopted. The resultant Mach numbers of each jet flow are $M_B = 0.80$ and $M_C = 0.59$. In terms of acoustic Mach number, where the jet velocities are divided by the speed of sound in the ambient flow, $M_{a_B} = 0.80$ and $M_{a_C} = 0.97$. For the cases with external flow, there is also a free-stream with velocity $U_f = 80$ m/s ($M_f = 0.23$). For the other cases, a free-stream condition is still added to the simulation domain, with a velocity of 1% of the bypass flow speed. This is done to ensure the dissipation of eddies that escape the jet shear layer. This free-stream speed can be considered negligible when compared to the jet velocities. Therefore, this condition will not alter the flow-field characteristics of the shear layer or the far-field noise results [16].

C. Sampling Regions

The flow-field properties are sampled on the engine symmetry plane (plane xy). For the far-field noise calculations, the information on unsteady flow properties is stored in a permeable Ffowcs Williams-Hawkings (FWH) surface, as shown in green in Fig. 4. It extends up to $23D_B$ in the axial direction, relative to the origin, with a maximum width of $7D_B$. Therefore, it is capable of capturing the noise from the jet quadrupoles, as well as from the dipoles distributed on the wing surfaces. Hydrodynamic perturbations occurring near the boundaries of the FWH must be avoided, since they contaminate the results with spurious sources of sound. Cutouts are then included at the engine and wing regions, from where the data is removed during the computations. In the axial direction, 7 outflow surfaces (or end-caps) are placed at the end of the FWH. The far-field pressure obtained from each cap is averaged, so that the spurious noise produced by the eddies crossing the FWH can be removed from the final far-field spectra [30].

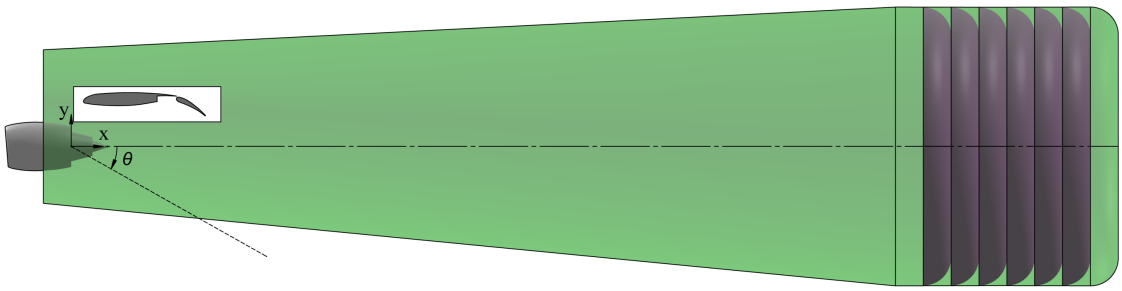

Fig. 4 Permeable surface with end-caps for far-field noise computation

The physical time of the simulations is divided into an initial transient, consisting of 5 flow passes through the FWH surface, and an acquisition time. The latter is defined based on the minimum output frequency to be analyzed (defined as $St = 0.1$), and the number of spectral averages (defined as 30), for an overlap coefficient of 0.5 in the Fast Fourier Transform (FFT) computation. Therefore, the physical time of the simulation is calculated as 2.32 s, with a minimum frequency resolution of 8.8 Hz. The unsteady pressure on the FWH surface is sampled with a frequency of 4.4 kHz, during 1.71 s of physical time acquisition.

The far-field noise levels are computed at a microphone arc array centered at the origin, as shown in Fig. 5. The radius of the array is defined as $100D_B$. Microphones are placed at an interval of 5°, ranging from $\theta = 15°$ to $\theta = 150°$ ($\theta = 0°$ corresponding to the jet axis). The computations are also performed on both shielded and reflected sides of the wing.

IV. Installation Effects on Jet Noise

A. Jet Velocity Profiles

In this section, installation effects on the dual-jet are assessed in the absence of external flow. Flow-field contour plots of the isolated and installed configurations are shown in Fig. 6. The plots display the time-averaged axial velocity, non-dimensionalized by the bypass jet nominal speed. The core and bypass flows can be distinguished, as well as a velocity increase near the intake lip due to the fan boundary condition. It is also shown that there is no grazing of the jet

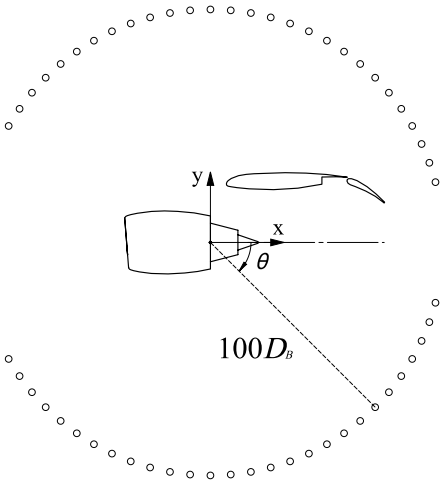

Fig. 5 Polar microphone array (Probe distance not to scale)

on the wing, and the flow is not deformed due to the presence of the solid surfaces. This can be confirmed through the centerline velocity profiles plotted for both configurations in Fig. 7. Small variations between upper and lower sides occur due to the discretization. Further refinement of the mesh would improve the flow axisymmetry.

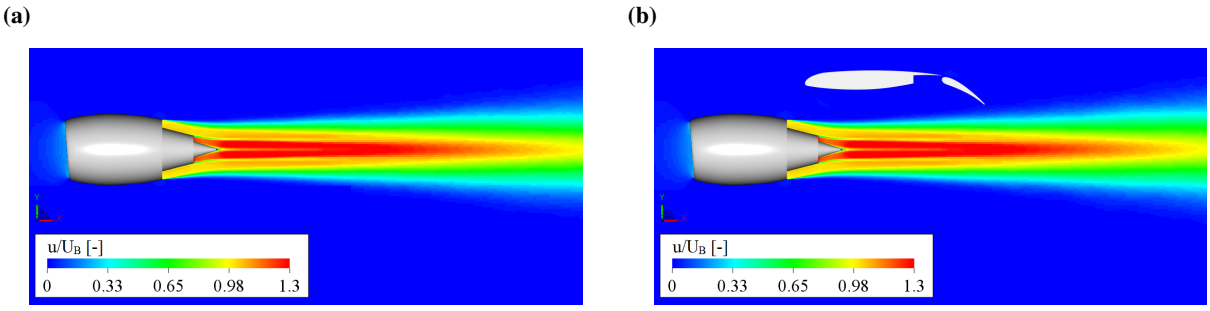

Fig. 6 Time-averaged $x-$velocity contour plots for isolated and installed jets without free-stream

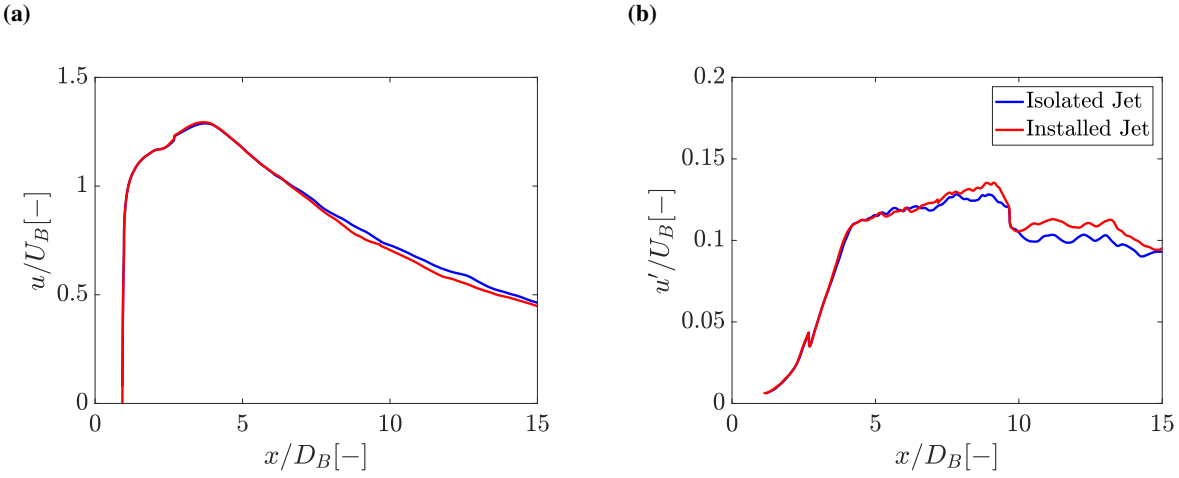

Fig. 7 Profiles of time-averaged and rms fluctuations of the centerline $x-$velocity for isolated and installed jets without free-stream

The centerline flow starts to develop around $x/D_B = 1.2$ and there is a progressive velocity increase up to $x/D_B = 3.7$. Theoretically, this region should display a constant velocity, corresponding to the potential core of the jet. However, due to the wake formed downstream of the engine center plug, the obtained values of the centerline velocity are less than the nominal speed of the core flow. For $x/D_B > 3.7$, there is a progressive velocity decay, which indicates the end of the potential core and the mixing of the two shear layers. This is also visible in Fig. 7b, where the velocity fluctuations increase rapidly up to the end of the potential core. The step at $x \approx 10D_B$ is caused by the change in mesh element size. Further refinement of the overall grid would reduce this effect. The profiles of isolated and installed jets are similar, confirming that the presence of the wing does not affect the steady properties of the jet.

B. Far-Field Spectra and Directivity

The far-field Sound Pressure Level (SPL) spectra for the isolated and installed jets are plotted in Fig. 8 for two polar angles: $\theta = 90°$, which corresponds to the sideline direction, and $\theta = 30°$, towards the jet axis. The narrowband spectra, obtained for a constant frequency band of 10 Hz, are displayed as a function of Strouhal number ($St = f \times D_B/U_B$), and for both reflected and shielded sides of the wing.

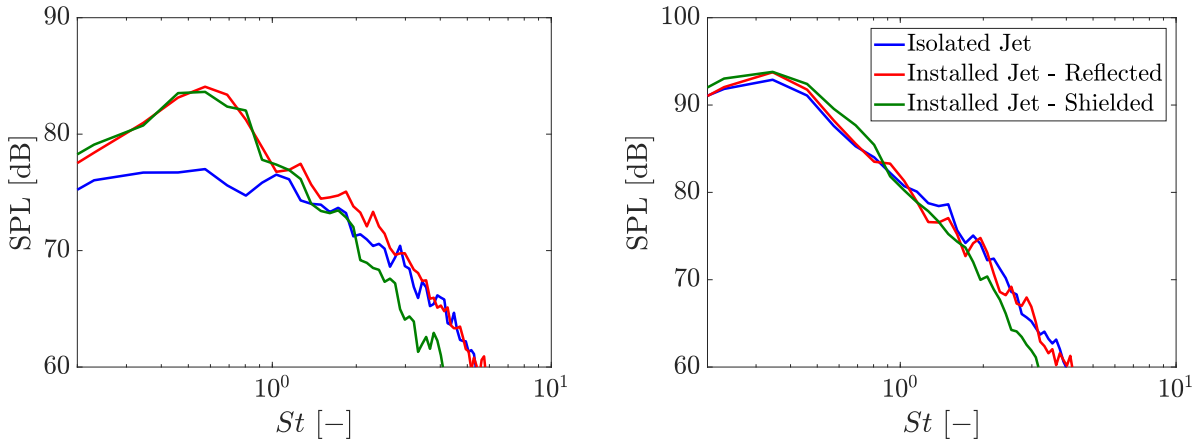

(a) $\theta = \pm 90°$ **(b)** $\theta = \pm 30°$

Fig. 8 Far-field spectra of isolated and installed jets in the absence of external flow, at different polar angles

In the sideline direction, installation effects are responsible for noise increases up to $St = 1$. The maximum amplification, relative to the isolated case, is 8 dB at $St = 0.7$. Up to $St = 1$, the spectra at the reflected and shielded sides display similar shape and amplitude, indicating that the dominant noise generation mechanism is the scattering of hydrodynamic waves at the flap trailing-edge. For $St > 1$, the spectra of the installed cases are dominated by the noise of quadrupole noise sources either reflected or shielded by the wing. At the reflected side, the noise levels are approximately 3 dB higher than the isolated case, as expected from the reflection on a half plane [6]. For $\theta = 30°$, i.e. towards the jet axis, installation effects are no longer dominant and the installed curves tend to collapse with the isolated one. The directivity of the isolated and installed jets is shown in Fig. 9, in terms of Overall Sound Pressure Level (OASPL), with the noise levels integrated for $0.2 < St < 4$.

For all configurations, the highest noise levels occur at $\theta = 35°$. The high Mach numbers of the bypass and core jets are responsible for strong quadrupole sources that dominate towards the jet axis. Moving upstream, the OASPL of the isolated jet decay rapidly compared to the installed one. Scattering at the flap trailing-edge is responsible for high noise levels, particularly in the upstream direction of the jet. There is a maximum difference of 7.5 dB at $\theta = 150°$ for the noise levels on the reflected side, with respect to the isolated case. The difference between shielded and reflected sides is more visible in the upstream direction, where the latter displays levels 6.5 dB higher than the former.

C. Noise Sources

The different sources and the radiated sound waves can be visualized through a time-derivative of the pressure field, as shown in Fig. 10. Contours are saturated to allow visualization of the pressure waves outside of the jet plume. The data are band-pass filtered in the frequency range $0.63 < St < 0.8$, which contains the spectral peak in the far-field plots.

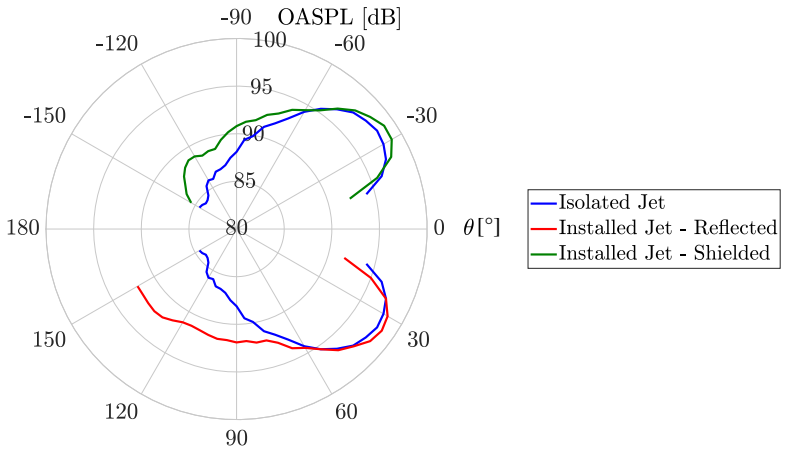

Fig. 9 Polar directivity of overall sound pressure levels for isolated and installed jets

It can be seen that pressure fluctuations are scattered at the flap trailing-edge and the waves propagate in a direction normal to the edge, as shown by the dashed line. This is consistent with the dipole behavior expected from this source [5]. Strong pressure fluctuations also propagate in the form of Mach waves. These waves are produced by quadrupole sources in the jet, and they have a strength comparable to that of the scattered waves due to the high Mach number of the jet flows. The dash-dotted lines represent an angle of 35°, relative to the jet axis, which is taken from the directivity plot. There is a good agreement between the direction of wave propagation and the far-field results.

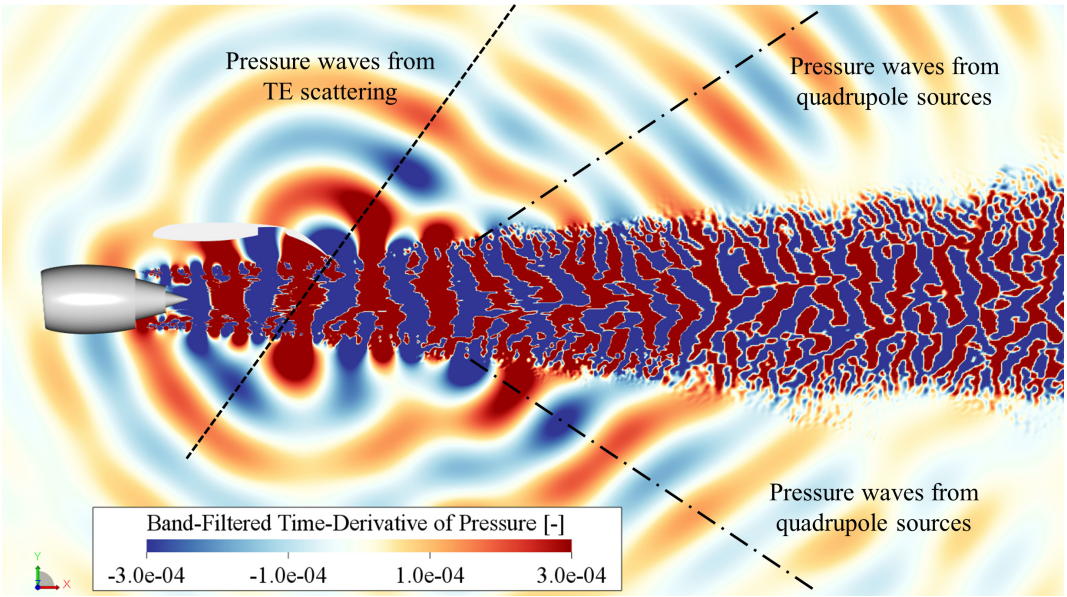

Fig. 10 Time derivative of the pressure field around the installed jet, for a frequency band of $0.63 < St < 0.8$

The contribution of each element to the overall noise levels is also assessed. The pressure fluctuations on each surface are integrated and propagated to the far-field via the solid FWH formulation [21]. Spectra for a polar angle $\theta = 90°$ (reflected side) are shown in Fig. 11a. The amplitude of pressure fluctuations is higher for the flap than the main element, with similar levels as the overall installed configuration near the spectral peak. This indicates that the scattering occurs only at the flap and the resultant noise produced by the main element is likely due to impingement of hydrodynamic and acoustic waves. Considering all these sources as uncorrelated, including the quadrupoles in the jet, their noise levels can be summed and compared to the results obtained from the permeable FWH surface, as shown in Fig. 11b. The curves collapse, indicating that there is no change to the quadrupole sources due to the presence of the wing.

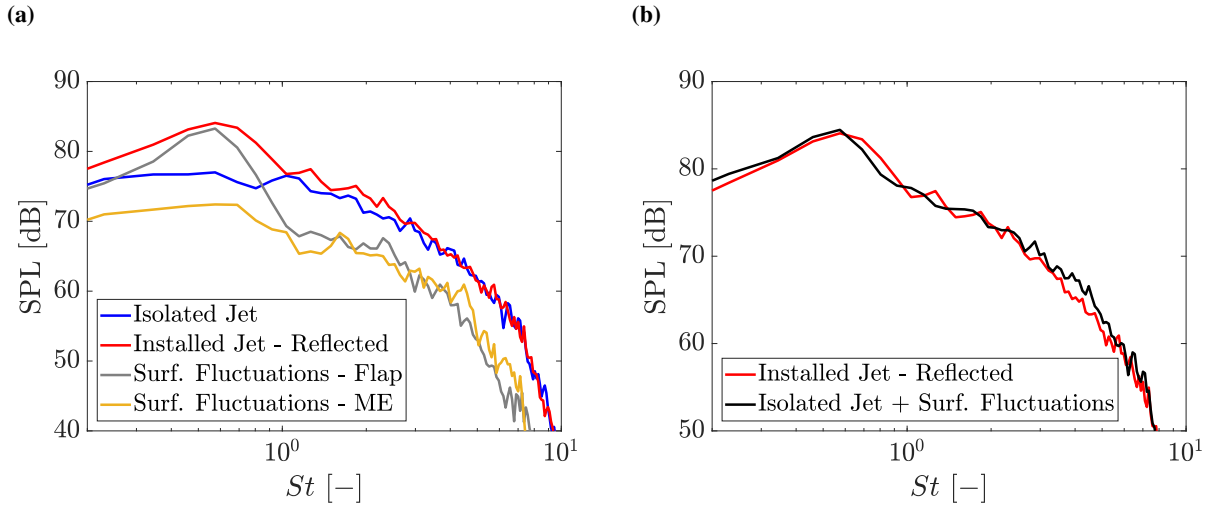

Fig. 11 Far-field levels computed from the pressure fluctuations at each surface component, compared to the overall installed noise

V. Free-Stream Effects on Jet-Installation Noise

A. Jet Velocity Profiles

In this section, a free-stream condition is added to the domain. Changes in the pressure field and development of the jet, and consequently the emitted noise, are expected due to this external flow. The contour plots shown in Fig. 12 display the time-averaged axial velocity of the dual jet. In Fig. 12a, there is again some asymmetry between upper and lower sides due to the low mesh resolution at that region. The most visible effect of the free-stream is seen in Fig. 12b for the installed configuration. There is a significant downward deflection of the jet flow, particularly visible downstream of the flap trailing-edge. This deflection is due to a vertical velocity component produced by the wing and it is likely to affect not only the quadrupole sources in the jet, but also the trailing-edge scattering of the jet hydrodynamic pressure waves. The profiles shown in Fig. 13 display more clearly the effect of free-stream on the jet centerline velocity.

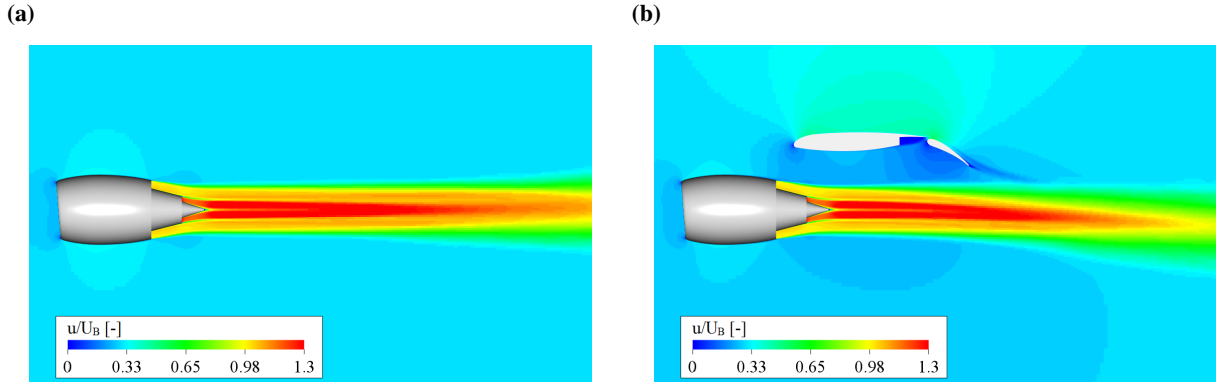

Fig. 12 Time-averaged $x-$velocity contour plots for isolated and installed jets with free-stream

Comparing both isolated cases (blue and green curves), it can be seen that the presence of free-stream slightly increases the potential core length and the downstream velocity decay is less steep. This indicates that the jet spreading angle is reduced, and the structures grow at a lower rate [12]. However, in the installed configuration, the downwash produced by the wing deflects the jet downwards, decreasing the velocity at the ceterline. The velocity fluctuations are also higher for the installed configuration, as seen in Fig. 13b. The step on the curves is due to the change in mesh element size.

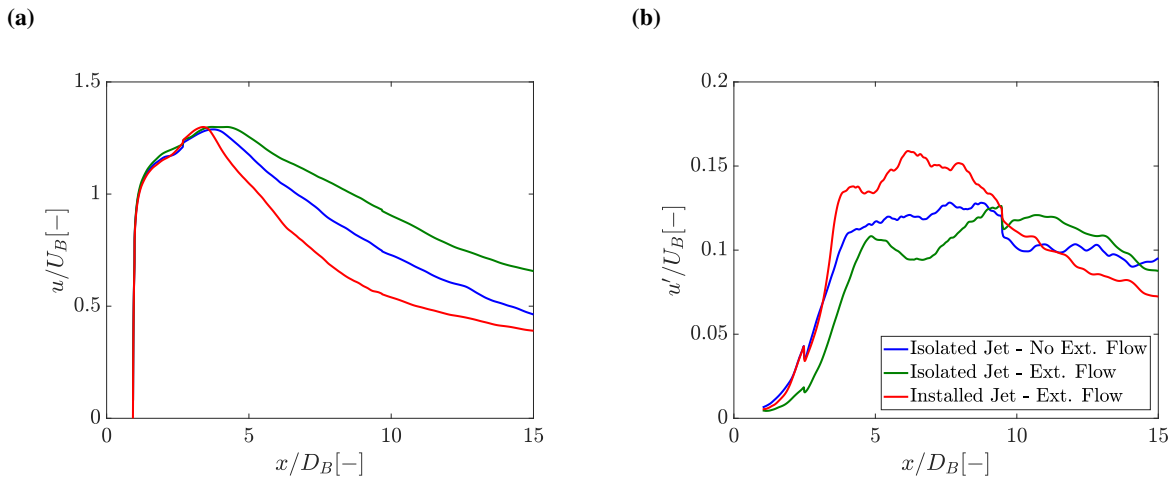

Fig. 13 Effect of free-stream on the time-averaged centerline $x-$velocity of isolated and installed jets

B. Far-field Spectra and Directivity

The far-field SPL spectra of the installed jets with and without free-stream are plotted in Fig. 14, for $\theta = 90°$ and $\theta = 120°$ (direction normal to the flap trailing-edge, on the reflected side). For $\theta = 90°$, comparing the spectra at the reflected and shielded sides for the case with free-stream, it can be seen that the curves collapse only in the frequency range of $0.45 < St < 0.6$. This indicates the range where the scattering of the jet hydrodynamic waves at the flap trailing-edge is the dominant noise mechanism. The reflected side curve resembles more an isolated jet spectrum, with no visible broadband hump, which indicates that the quadrupole sources are stronger in this direction due to the deflection of the plume. For $\theta = 120°$, it is shown that the addition of free-stream reduces the levels of the broadband hump at the reflected side, but there is noise increase at mid frequencies ($St \approx 0.8$). At high frequencies, the curves of both cases display similar levels, indicating that the quadrupole sources at these frequencies are not significantly affected by the plume deflection.

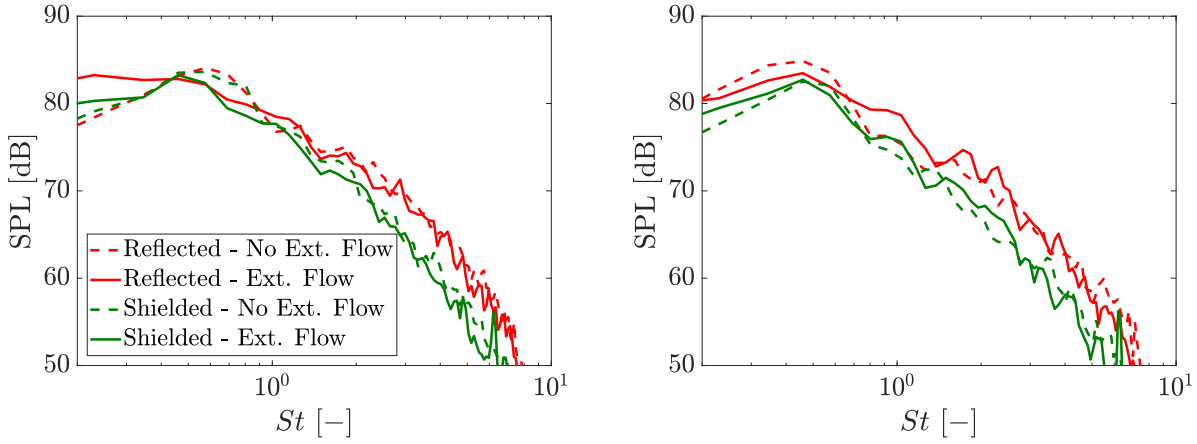

(a) $\theta = \pm 90°$ **(b)** $\theta = \pm 120°$

Fig. 14 Far-field spectra of the installed jet with and without free-stream

The overall directivity of the installed configuration is also altered by the presence of free-stream, as shown in Fig. 15. The maximum OASPL shifts from $\theta = 35°$ to $\theta = 45°$. This is likely to occur due to convection effects, which shifts the wave propagation towards the upstream direction. For higher polar angles, the curves display similar levels, since the reduction on the scattered noise is compensated with an increase at lower and higher frequencies from quadrupole sources.

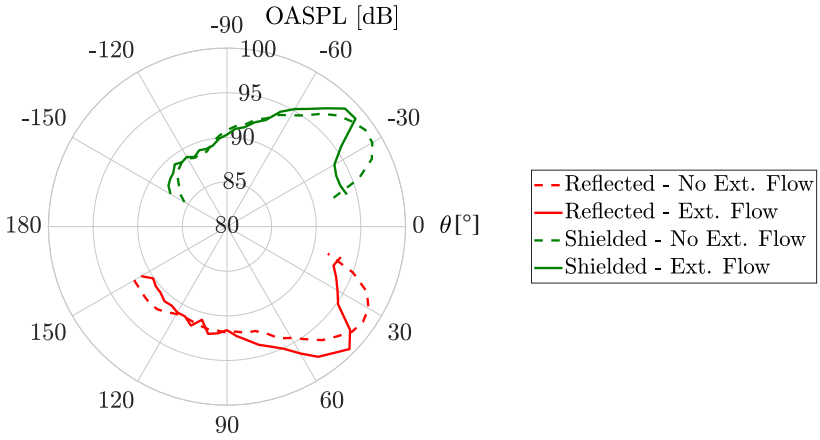

Fig. 15 Polar directivity of overall sound pressure levels for installed jets with and without free-stream

C. Noise Sources

The time-derivative of the pressure field for the installed configuration with free-stream is plotted in Fig. 16. The data are again band-passed to a frequency range $0.63 < St < 0.8$. For this configuration, the waves scattered at the flap trailing-edge are still visible, propagating normal to the flap surface. The sound waves generated by the quadrupole sources are also visible, following the dash-dotted lines, which have an angle of 45°, relative to the jet axis. These results are in agreement with the far-field directivity. For this case, the main noise source is placed farther downstream than the previous one without free-stream. This occurs due to the change in the position where the outer shear layers merge, which is moved downstream for the cases with free-stream. The fluctuations outside of the plume also have lower amplitudes than those in the absence of free-stream, indicating the reduced energy content of the structures that generate them.

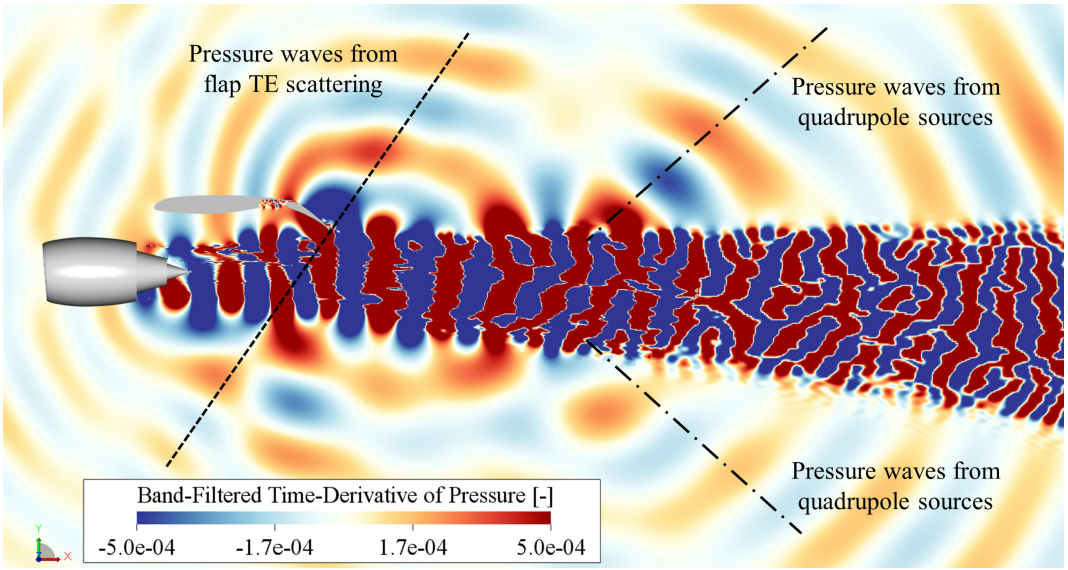

Fig. 16 Time-derivative of the pressure field around the installed jet + free-stream, for a frequency band of $0.63 < St < 0.8$

The contribution of each element to the overall installed noise levels is shown in Fig. 17a, for a polar angle $\theta = 90°$ (reflected side). The amplitude of pressure fluctuations on the flap is higher than that of the main element up to $St = 0.9$. However, for this case, the noise generated by the flap approaches the overall installed curve only in the frequency range of $0.45 < St < 0.7$, which is compatible to the region where the noise at the shielded and reflected sides are similar. For $St > 0.9$, the noise generated by the main element becomes dominant over that produced by the flap, since the

amplitude of the latter decays rapidly. A comparison of the spectra of surface pressure fluctuations for both cases is shown in Fig. 17b. Up to $St = 0.5$, the amplitude of pressure fluctuations on the flap are similar for both cases. This frequency also corresponds to the spectral peak for the case with free-stream. There is a reduction of the broadband hump, as well as the amplitude of fluctuations at high frequencies, which are likely related to a reduced strength of the quadrupole sources due to the presence of free-stream. For the main element, there is a slight increase in pressure fluctuations with flow present, which are likely related to turbulent boundary-layer trailing-edge noise.

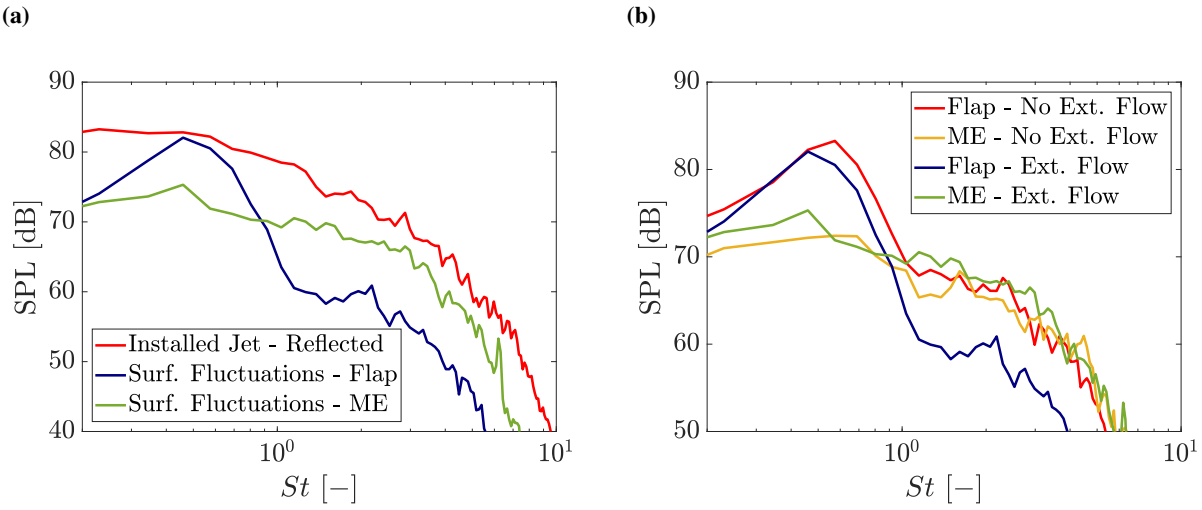

Fig. 17 Far-field levels computed from the pressure fluctuations at each surface component with and without free-stream

D. Wavelet Decomposition

In this section, a decomposition technique based on the wavelet transform is used to assess the phenomena behind the different noise characteristics with respect to the presence of free-stream. This technique has been proposed by Mancinelli et al. [31] with the aim to separate the coherent part in a flow from that with a more chaotic characteristic. The coherent flow structures, in the form of instability waves, display strong hydrodynamic behavior, whereas the chaotic ones are usually linked to acoustic fluctuations. The aim of this analysis is to remove the contribution of the scattered waves in the near-pressure field so that only the hydrodynamic content from the quadrupoles is assessed. The technique applied in this work is based on a recursive de-noising procedure (WT3), in which the acoustic pressure field is iteratively evaluated until a convergence criterion is satisfied, based on the wavelet coefficients being higher or lower than a threshold [31]. A default set of wavelet (Daubechies-12 type) and a unitary threshold coefficient are used for the decomposition of the near-field pressure around the dual-jet. This technique has been also applied by van der Velden et al. [15] for a single-stream hot jet, where coherent structures and radiating Mach waves have been educed. The contour plots in Fig. 18 display the decomposed near-pressure field into coherent (left) and chaotic (right) components, at a frequency range of $0.63 < St < 0.8$, for the cases without and with free-stream, respectively.

From the plots, it can be seen that inside of the plume, where non-linear effects are present, the characteristics of the two types of fluctuations cannot be distinguished. Outside of this region, the coherent and chaotic fluctuations have hydrodynamic and acoustic characters, respectively. The coherent field is fairly strong, particularly at the outer shear layer, but tends to decay faster when moving away from the plume. The fluctuations in the chaotic field, on the other hand, persist farther from the plume and resemble Mach waves radiating to the far-field, similarly as shown in the dilatation field plots. Acoustic fluctuations are also generated at the flap trailing-edge due to scattering of the impinging hydrodynamic waves, and move also upstream of the jet axis. Comparing the coherent fields of the cases without and with free-stream, the waves propagating in the downstream direction appear to be weaker for the latter. This is likely due to the reduced shear stresses from the presence of free-stream, which in turn reduces the energy of fluctuations at this frequency. A convective effect due to the presence of free-stream is also visible by waves propagating in the upstream direction. The two chaotic fields, on the other hand, do not display significant differences from each other.

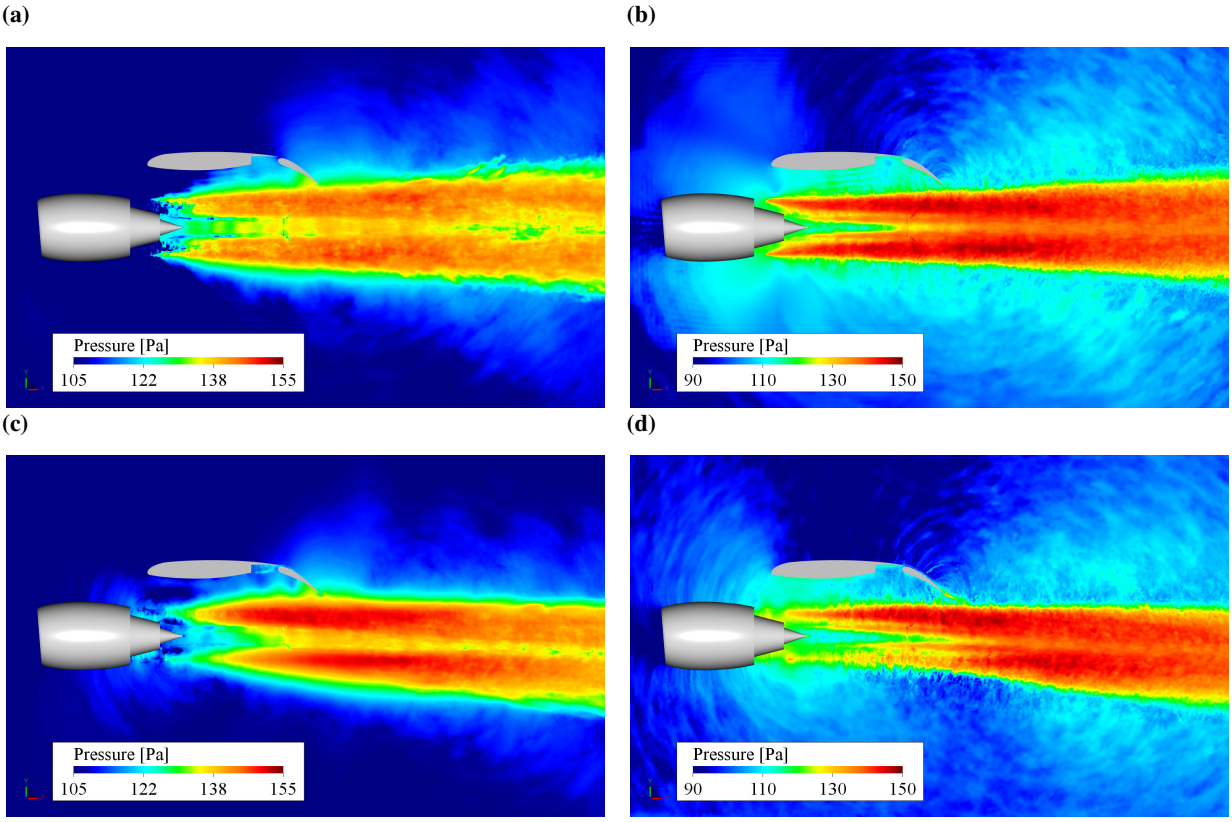

Fig. 18 Decomposed pressure field into coherent (left) and chaotic (right) components for cases without (a,b) and with (c,d) free-stream and for a frequency range $0.63 < St < 0.8$

The wavelet decomposition is also applied to pressure signals obtained from near-field probes, situated outside of the plume. The first probe is positioned at $(x_1, y_1) = (3D_B, 0.7D_B)$, i.e. in between the jet and the wing, close to the flap trailing-edge. The second probe is positioned further downstream, at $(x_2, y_2) = (10D_B, 1.6D_B)$. The spectra of the decomposed signals are shown in Fig. 19. For these probes, the hydrodynamic and acoustic character of the fluctuations can be properly educed. The results show that the hydrodynamic component is dominant at low frequencies, overlapping with the overall curve, whereas the acoustic fluctuations are dominant at high frequencies. The former is a result of the coherent structures present in the jet shear layer, which usually have large wavelengths, whereas the latter is associated with the Mach waves produced by the jet, and those scattered at the flap trailing-edge. Comparing the two probes, it can be seen that, by moving downstream in the jet axis, the cross-over between hydrodynamic and acoustic fluctuations occurs at lower frequencies. These results are in agreement with Mancinelli et al. [31] and van der Velden et al. [15].

The hydrodynamic and acoustic components of the probes pressure signals are compared for the cases with and without free-stream. By comparing only the hydrodynamic part, it is possible to verify how the pressure waves from the quadrupole sources are affected by the presence of free-stream. Two more probes are added, at the same axial position of the previous ones, but on the lower side: $(x_3, y_3) = (3D_B, -0.7D_B)$ and $(x_4, y_4) = (10D_B, -1.6D_B)$, since the jet is no longer axisymmetric when there is free-stream. Their spectra are shown in Fig. 20.

In the first set of spectra (Fig. 20a), it is shown that the hydrodynamic components of both cases are approximately similar, and the case without free-stream displaying slightly higher levels. This is likely caused by the reduced shear stresses, which in turn also reduce the level of the fluctuations. This behavior is also seen in the acoustic components. Moving downstream, this effect becomes more apparent, as shown in Fig. 20b. The hydrodynamic fluctuations are much stronger for the case without free-stream, whereas the acoustic components become similar. For the probes on the lower side, the spectra display different trends. Due to the deflection of the jet in that direction for the case with free-stream, the fluctuations become stronger and are comparable to the other case. At downstream positions (Fig. 20d), the levels of both hydrodynamic and acoustic components are higher for the case with free-stream, which is in agreement with the results from the far-field analysis.

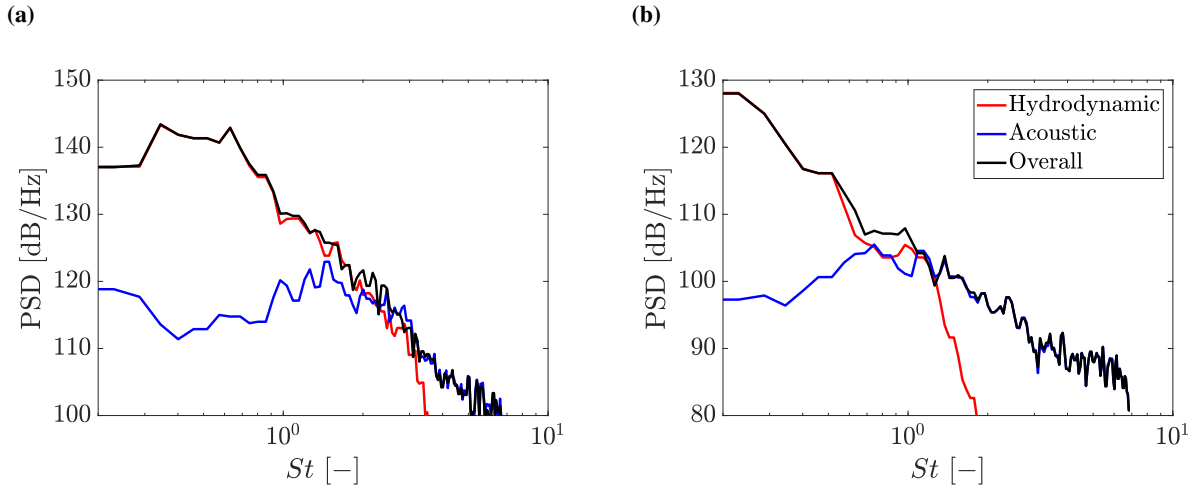

Fig. 19 Hydrodynamic and acoustic components of the pressure signal at two probes located outside of the jet plume

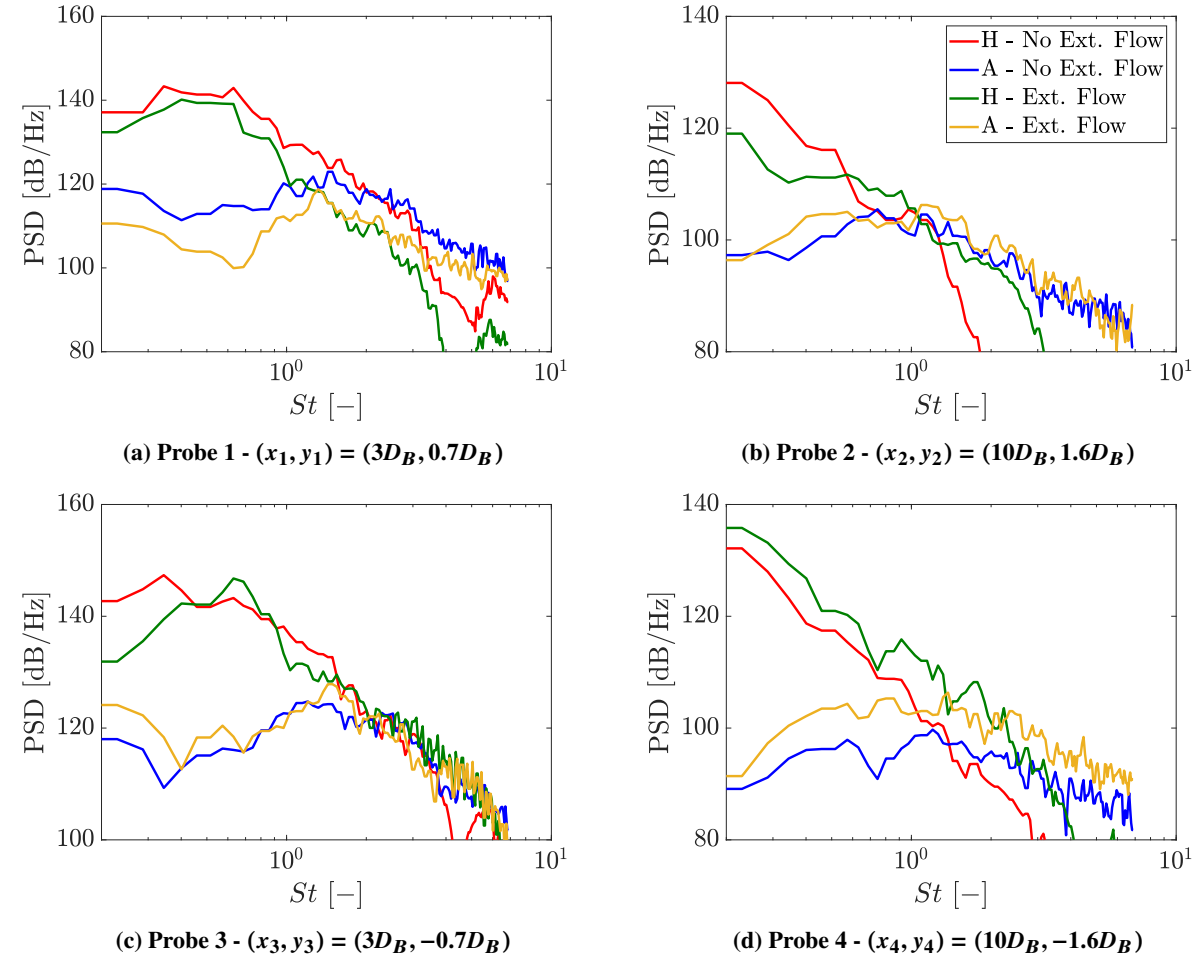

(a) Probe 1 - $(x_1, y_1) = (3D_B, 0.7D_B)$

(b) Probe 2 - $(x_2, y_2) = (10D_B, 1.6D_B)$

(c) Probe 3 - $(x_3, y_3) = (3D_B, -0.7D_B)$

(d) Probe 4 - $(x_4, y_4) = (10D_B, -1.6D_B)$

Fig. 20 Comparison of hydrodynamic and acoustic components of the pressure signal for cases without and with free-stream

VI. Conclusions

A high-fidelity numerical investigation of free-stream effects on jet-installation noise was performed using the lattice-Boltzmann method. A realistic full-scale configuration, comprised by a dual-jet engine and a flapped wing, was chosen for the analyses. The jet flows were simulated based on input conditions for the engine at take-off, and the wing was placed in the vicinity of the engine at a distance to avoid direct grazing.

The installation effects were initially investigated in the absence of free-stream. The far-field spectral results in the sideline direction, obtained from the Ffowcs-Williams and Hawkings analogy, indicated a large noise increase at low frequencies, followed by reflection or shielding of the quadrupole jet noise. Through dilatation field plots, this amplification was shown to be caused by the hydrodynamic waves from the jet that are scattered at the flap trailing-edge to the far-field as noise. This new source displayed maximum noise levels in the upstream direction of the jet axis, whereas in the downstream direction, the noise was similar to that of the isolated configuration. Through integration of surface pressure fluctuations on each wing component, it was found that the flap is indeed responsible for the broadband hump at low frequencies. By considering the surface dipoles and the quadrupoles in the jet as uncorrelated sources, their noise levels were summed and the result matched the overall installed spectra. This showed that the presence of the wing did not alter the structures in the jet shear layer, in this case.

When free-stream was added to the computations, different results were obtained. In an isolated jet, the presence of a free-stream was responsible for an elongation of the potential core and a lower centerline velocity decay. However, for the installed jet, an opposite result was obtained. Due to the downwash produced by the wing, the jet plume deflected downward, which in turn affected the characteristics of the noise sources. While the broadband hump was slightly reduced, there was additional noise at low and mid frequencies, compared to the case without free-stream, particularly on the reflected side of the wing.

A wavelet decomposition was performed on the near-pressure field in order to separate the contributions from coherent and chaotic fluctuations. The reduction of the broadband hump was attributed to less energetic structures (less coherent content) upstream of the flap trailing-edge, in comparison to the case without flow. On the lower side of the plume, the structures were found to be more energetic due to the plume deflection, generating stronger fluctuations, which is in agreement with the far-field results. Further research on this topic includes addressing the effect of the jet flow properties, different flap deflection angles and the presence of a slat (for a condition with angle of attack between the geometry and the free-stream) on the installation noise of a full-scale dual jet.

Acknowledgments

This work is part of the IPER-MAN project (**I**nnovative **PER**meable **M**aterials for **A**irfoil **N**oise Reduction), project number 15452. The authors would like to thank Dr. Mirjam Snellen and Prof. Sybrand van der Zwaag for collaboration in the project.

References

[1] Huff, D. L., "Noise Reduction Technologies for Turbofan Engines," *NASA/TM—2007-214495*, 2007, pp. 1–17.

[2] SenGupta, G., "Analysis of Jet-Airframe Interaction Noise," *8th AlAA Aeroacoustics Conference*, Atlanta, GA, USA, 1983.

[3] Brown, W. H., and Ahuja, K. K., "Jet and Wing/Flap Interaction Noise," *AIAA/NASA 9th Aeroacoustics Conference*, WiIIiamsburg, VA, USA, 1984. doi:10.2514/6.1984-2362.

[4] Ffowcs-Williams, J. E., and Hall, L. H., "Aerodynamic sound generation by turbulent flow in the vicinity of a scattering half plane," *Journal of Fluid Mechanics*, Vol. 40, No. 4, 1970, pp. 657–670. doi:10.1017/S0022112070000368.

[5] Head, R. W., and Fisher, M. J., "Jet/Surface Interaction Noise: - Analysis of Farfield Low Frequency Augmentations of Jet Noise due to the presence of a Solid Shield," *3rd AIAA Aero-Acoustics Conference*, Palo Alto, CA, USA, 1976. doi:10.2514/6.1976-502.

[6] Cavalieri, A. V. G., Jordan, P., Wolf, W. R., and Gervais, Y., "Scattering of wavepackets by a flat plate in the vicinity of a turbulent jet," *Journal of Sound and Vibration*, Vol. 333, No. 24, 2014, pp. 6516–6531. doi:10.1016/j.jsv.2014.07.029.

[7] Roger, M., Moreau, S., and Kucukcoskun, K., "On sound scattering by rigid edges and wedges in a flow, with applications to high-lift device aeroacoustics," *Journal of Sound and Vibration*, Vol. 362, 2016, pp. 252–275. doi:10.1016/j.jsv.2015.10.004.

[8] Lyu, B., Dowling, A. P., and Naqavi, I., "Prediction of installed jet noise," *Journal of Fluid Mechanics*, Vol. 811, 2017, pp. 234–268. doi:10.1017/jfm.2016.747.

[9] Mead, C. J., and Strange, P. J. R., "Under-Wing Installation effects on Jet Noise at Sideline," *4th AIAA/CEAS Aeroacoustics Conference*, Toulouse, France, 1998. doi:10.2514/6.1998-2207.

[10] Mengle, V. G., Brusniak, L., Elkoby, R., and Thomas, R. H., "Reducing Propulsion Airframe Aeroacoustic Interactions with Uniquely Tailored Chevrons: 3. Jet-Flap Interaction," *12th AIAA/CEAS Aeroacoustics Conference*, Cambridge, MA, USA, 2006. doi:10.2514/6.2006-2435.

[11] Belyaev, I., Faranosov, G., Ostrikov, N., and Paranin, G., "A parametric experimental study of jet-flap interaction noise for a realistic small-scale swept wing model," *21st AIAA/CEAS Aeroacoustics Conference*, Dallas, TX, USA, 2015. doi: 10.2514/6.2015-2690.

[12] Proença, A. R., "Aeroacoustics of Isolated and Installed Jets under Static and In-Flight Conditions," Ph.D. thesis, University of Southampton, UK, 2018.

[13] Stanford University AA283 Course Material, *The GE90 - An Introduction.pdf*, 1995.

[14] Murayama, M., Nakakita, K., Yamamoto, K., Ura, H., Ito, Y., and Choudhari, M., "Experimental Study of Slat Noise from 30P30N Three-Element High-Lift Airfoil in JAXA Hard-Wall Low-Speed Wind Tunnel," *20th AIAA/CEAS Aeroacoustics Conference*, 2014. doi:10.2514/6.2014-2080.

[15] van der Velden, W. C. P., Casalino, D., Gopalakrishnan, P., Jammalamadaka, A., Li, Y., Zhang, R., and Chen, H., "Jet Noise Prediction : Validation and Physical Insight," *24th AIAA/CEAS Aeroacoustics Conference*, Atlanta, GA, USA, 2018, pp. 1–16.

[16] Rego, L., Avallone, F., Ragni, D., and Casalino, D., "Numerical Analysis of Installation Noise on a Jet-Flat Plate Configuration," *AIAA SciTech Forum, to be published*, San Diego, CA, 2019.

[17] Nickerson, M. L., Ferris, R., and van der Velden, W. C. P., "Simulations of Chevrons on Single Flow Hot Jets," *AIAA SciTech Forum*, American Institute of Aeronautics and Astronautics (AIAA), San Diego, CA, USA, 2019. doi:10.2514/6.2019-1837.

[18] Succi, S., *The lattice Boltzmann equation for fluid dynamics and beyond*, Oxford University Press, New York, NY, USA, 2001.

[19] Chen, H., Gopalakrishnan, P., and Zhang, R., "Recovery of Galilean Invariance in Thermal Lattice Boltzmann Models for Arbitrary Prandtl Number," *International Journal of Modern Physics C*, Vol. 25, No. 10, 2014. doi:10.1142/S0129183114500466.

[20] Yakhot, V., and Orszag, S. A., "Renormalization group analysis of turbulence. I. Basic theory," *Journal of Scientific Computing*, Vol. 1, No. 1, 1986, pp. 3–51. doi:10.1007/BF01061452.

[21] Ffowcs-Williams, J. E., and Hawkings, D. L., "Sound Generation by Turbulence and Surfaces in Arbitrary Motion," *Philosophical Transactions of the Royal Society A: Mathematical, Physical and Engineering Sciences*, Vol. 264, No. 1151, 1969, pp. 321–342. doi:10.1098/rsta.1969.0031.

[22] Brès, G., Pérot, F., and Freed, D., "A Ffowcs Williams - Hawkings Solver for Lattice-Boltzmann Based Computational Aeroacoustics," *16th AIAA/CEAS Aeroacoustics Conference*, Stockholm, Sweden, 2010. doi:10.2514/6.2010-3711.

[23] Farassat, F., and Succi, G. P., "A review of propeller discrete frequency noise prediction technology with emphasis on two current methods for time domain calculations," *Journal of Sound and Vibration*, Vol. 71, No. 3, 1980, pp. 399–419. doi:10.1016/0022-460X(80)90422-8.

[24] Casalino, D., "An advanced time approach for acoustic analogy predictions," *Journal of Sound and Vibration*, Vol. 261, No. 4, 2003, p. 583–612. doi:10.1016/S0022-460X(02)00986-0.

[25] Casalino, D., Hazir, A., and Mann, A., "Turbofan Broadband Noise Prediction Using the Lattice Boltzmann Method," *AIAA Journal*, Vol. 56, No. 2, 2017, pp. 609–628. doi:10.2514/1.J055674.

[26] Casalino, D., Avallone, F., Gonzalez-Martino, I., and Ragni, D., "Aeroacoustic study of a wavy stator leading edge in a realistic fan/OGV stage," *Journal of Sound and Vibration*, Vol. 442, 2019, pp. 138–154. doi:10.1016/j.jsv.2018.10.057, URL `https://doi.org/10.1016/j.jsv.2018.10.057`.

[27] Gonzalez-Martino, I., and Casalino, D., "Fan Tonal and Broadband Noise Simulations at Transonic Operating Conditions Using Lattice-Boltzmann Methods," *2018 AIAA/CEAS Aeroacoustics Conference*, Atlanta, GA, USA, 2018. doi:10.2514/6.2018-3919.

[28] Colonius, T., Lele, S. K., and Moin, P., "Sound generation in a mixing layer," *Journal of Fluid Mechanics*, Vol. 330, 1997, pp. 375–409. doi:10.1017/S0022112096003928.

[29] Blumenthal, B., Elmiligui, A. A., Geiselhart, K., Campbell, R. L., Maughmer, M. D., and Schmitz, S., "Computational Investigation of a Boundary Layer Ingestion Propulsion System for the Common Research Model," *46th AIAA Fluid Dynamics Conference*, 2016. doi:10.2514/6.2016-3812.

[30] Brès, G., Nichols, J. W., Lele, S., and Ham, F. E., "Towards Best Practices for Jet Noise Predictions with Unstructured Large Eddy Simulations," *42nd AIAA Fluid Dynamics Conference and Exhibit*, New Orleans, LA, USA, 2012.

[31] Mancinelli, M., Pagliaroli, T., Di Marco, A., Camussi, R., and Castelain, T., "Wavelet decomposition of hydrodynamic and acoustic pressures in the near field of the jet," *Journal of Fluid Mechanics*, Vol. 813, 2017, pp. 716–749. doi: 10.1017/jfm.2016.869.